Biomacromolecules

pubs.acs.org/Biomac

Article

Alignment–Rheology Relationship of Biosourced Rod-Like Colloids and Polymers under Flow

Marvin Detert,* Tatiana Porto Santos, Amy Q. Shen, and Vincenzo Calabrese*

Cite This: *Biomacromolecules* 2023, 24, 3304–3312

Read Online

ACCESS | Metrics & More | Article Recommendations | Supporting Information

ABSTRACT: Fluids composed of biosourced rod-like colloids (RC) and rod-like polymers (RP) have been extensively studied due to various promising applications relying on their flow-induced orientation (e.g., fiber spinning). However, the relationship between RC and RP alignment and the resulting rheological properties is unclear due to experimental challenges. We investigate the alignment–rheology relationship for a variety of biosourced RC and RP, including cellulose-based particles, filamentous viruses, and xanthan gum, by simultaneous measurements of the shear viscosity and fluid anisotropy under rheometric shear flows. For each system, the RC and RP contribution to the fluid viscosity, captured by the specific viscosity η_{sp}, follows a universal trend with the extent of the RC and RP alignment independent of concentration. We further exploit this unique rheological-structural link to retrieve a dimensionless parameter (β) directly proportional to η_{sp} at zero shear rate ($\eta_{0,sp}$), a parameter often difficult to access from experimental rheometry for RC and RP with relatively long contour lengths. Our results highlight the unique link between the flow-induced structural and rheological changes occurring in RC and RP fluids. We envision that our findings will be relevant in building and testing microstructural constitutive models to predict the flow-induced structural and rheological evolution of fluids containing RC and RP.

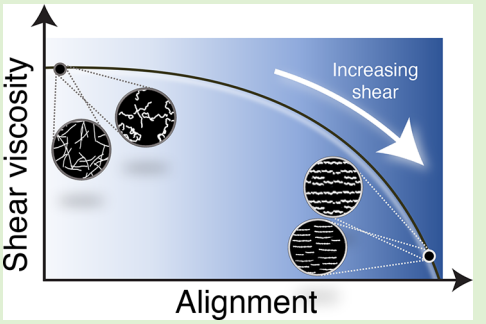

INTRODUCTION

Biosourced rod-like colloids (RC) and rod-like polymers (RP) have excellent mechanical and optical properties and are often regarded as sustainable and biocompatible building blocks.[1−7] These features have been exploited to form novel materials[8−10] with applications in biomedical[11−14] and food engineering.[15−20] Classical examples of biosourced RC that can be produced in industrially relevant quantities comprise cellulose nanofibrils, cellulose nanocrystals, and protein nanofibrils. Nonetheless, these RC are characterized by a polydisperse contour length which complicates the prediction of their flow behavior. In contrast, filamentous viruses are monodisperse RC suited for fundamental studies regarding the dynamics of rod-like object dispersions.[21,22] Biosourced RP comprises a myriad of polyelectrolytes, including xanthan gum, carboxymethyl cellulose, and hyaluronic acid, in aqueous environments that promote a rod-like conformation of the polymer chain (i.e., salt-free solutions at pH far from the isoelectric point of the functional group).[23] In most applications (e.g., inkjet printing, extrusion, and fiber spinning), controlling the flow-induced orientation and the resulting rheological properties of RC dispersions and RP solutions is crucial to achieve the desired functional and mechanical properties. The shear rheology of biosourced RC and RP fluids has been investigated extensively.[24−28] However, the link between RC and RP alignment and the resulting rheological properties (e.g., shear viscosity) has not yet been completely elucidated. On this front, using rheo-small angle neutron scattering (rheo-SANS), Förster et al.[29] showed a direct relationship between the shear viscosity (η) and the orientational order of worm-like micelles and elongated block copolymers under rheometric shear flow. Specifically, all the systems investigated by Förster et al.[29] followed a unique exponential decrease of η with the enhanced particle alignment, captured by the structural order parameter (S), as $\eta \propto e^{-AS}$, with A being an empirical fitting parameter. A similar exponential relationship was shown for monodisperse filamentous viruses by Lang et al. using a rheo-SANS setup.[30,31] More recently, Calabrese et al.,[32] coupling microfluidics with flow-induced birefringence (FIB) could verify the exponential viscosity decay with the increasing extent of particle alignment, in analogy with the studies of Förster et al.[29] and Lang et al.[30,31] Nonetheless, it is unclear to what extent this exponential relationship is a general feature of RC and RP fluids. In other studies, the extent of RC/RP alignment and the resulting shear viscosity have been investigated (via FIB and rheo-scattering) but have not been directly linked.[33−38] In the present work we explore the relationship between RC and RP alignment and the resulting rheological

Received: April 5, 2023
Revised: May 18, 2023
Published: June 26, 2023

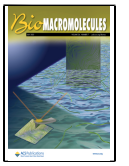

properties (alignment−rheology relationship) for a wide variety of naturally derived RC and RP with significantly distinct morphology, length scales, and flexibility. As model biosourced RC, we use cellulose nanocrystals (CNC), TEMPO-oxidized cellulose nanofibrils (OCNF) with two different average contour lengths, and a filamentous virus (*Pseudomonas* phage, Pf1). As biosourced RP, we use the polyelectrolyte xanthan gum (XG) in salt-free aqueous solutions. In this medium, the XG chains adopt a rod-like conformation due to intrachain electrostatic repulsion.[39,40]

Rigid Rod Theory. A suitable theoretical framework to describe the behavior of RC dispersions and RP solutions is given by the Doi−Edwards (DE) theory developed for monodisperse rigid rods in a continuum medium.[41,42] The DE theory defines distinct concentration regimes based on the number of rod-like objects per unit volume, $\nu = (4\phi)/(d^2L\pi)$ (in m^{-3}), where L is the contour length, d is the diameter, and ϕ the volume fraction of the particles. The onset of the semidilute regime is defined as $\nu^* = L^{-3}$, while the onset of the concentrated regime is $\nu^{**} = L^{-2}d^{-1}$. Alternatively, ν^* and ν^{**} can be expressed in terms of concentration (c) with units of mg/mL as $c^* = \rho_p\pi d^2/(4L^2)$ and $c^{**} = \rho_p\pi d/(4L)$, respectively, by knowing the particle density (ρ_p). In the dilute regime (i.e., $\nu/\nu^* = c/c^* < 1$), the rotational diffusion coefficient is $Dr \equiv Dr_0 = \frac{3k_bT\ln(L/d)}{\pi\eta_sL^3}$, where k_b is the Boltzmann constant, T is the absolute temperature, and η_s is the solvent viscosity.[41] Importantly, Dr_0 does not account for interparticle interactions; thus, it is independent of the particle concentration (see dashed line in Figure 1). In the semidilute regime (i.e., $\nu^* < \nu < \nu^{**}$), the DE theory assumes the rods as confined in an imaginary tube, where the tube represents the available space for the rods to rotate along their main axis unconstrained by the neighboring rods.[41] In this regime, the DE theory gives the rotational diffusion coefficient as[41,42]

$$Dr = Dr_0K(\nu L^3)^{-2} \quad (1)$$

where K is a dimensionless prefactor dictating the scaling transition from dilute to semidilute regime. From the simulation and experiments of monodisperse and rigid RC, it has been reported that $K = 1300$.[21,31,43] However, RC flexibility has been shown to affect K. Indeed, for the semiflexible Pf1, $K = 2300$ has been reported.[21,31] The DE theory gives the zero-shear rate specific viscosity $\eta_{0,sp}$ as[31,44]

$$\eta_{0,sp} = \frac{(\eta_0 - \eta_s)}{\eta_s} = \frac{\nu\pi L^3}{90\ln L/(2d)} + \frac{\nu^3\pi L^9}{30K\ln L/(2d)} \quad (2)$$

where η_0 is the limiting shear viscosity at $\dot{\gamma} \to 0$. Plotting $\eta_{0,sp}$ as a function of $\nu/\nu^* = c/c^*$, considering a representative rod-like particle (L = 1000 nm and d = 3 nm) and K = 1300 in eq 2, two distinct regimes are observed (Figure 1). At relatively low concentrations, $\eta_{0,sp} \propto \nu/\nu^* = c/c^*$, while at relatively high concentrations, $\eta_{0,sp} \propto (\nu/\nu^*)^3 = (c/c^*)^3$ (see Figure 1). Importantly, $\eta_{0,sp}$ follows the dilute scaling up to $\nu/\nu^* = c/c^* \sim 10$. This indicates that the rod-like particles are practically unconfined up to $\nu/\nu^* = c/c^* \sim 10$. At $\nu/\nu^* = c/c^* \gtrsim 40$, the rod-like particles are confined by the neighboring particles, following the scaling $\eta_{0,sp} \propto (\nu/\nu^*)^3 = (c/c^*)^3$ based on the tube assumption. Analogous to $\eta_{0,sp}$, the Dr/Dr_0 scaling (solid blue line in Figure 1, based on eq 1) intercepts with Dr_0 at $\nu/\nu^* = c/c^* \sim 40$, implying that the rod-like particles interact significantly with each other at $\nu/\nu^* = c/c^* \gtrsim 40$.[21] The scalings $Dr/Dr_0 \propto (\nu/\nu^*)^{-2}$ and $\eta_{0,sp} \propto (\nu/\nu^*)^3$ are expected to be valid in the limiting case where the underlying tube assumption, from the DE theory, holds (see Figure 1).

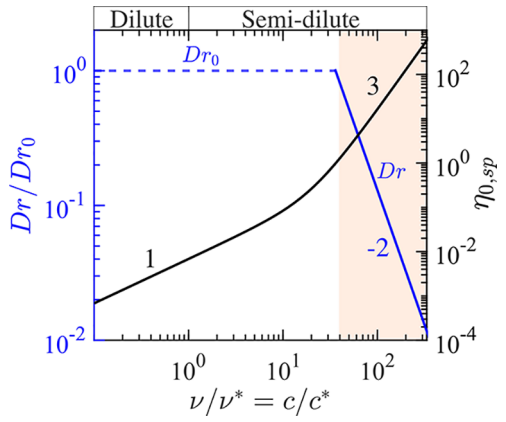

Figure 1. Theoretical normalized rotational diffusion coefficient (Dr/Dr_0, solid blue line) and zero-shear rate specific viscosity ($\eta_{0,sp}$, solid black line). The Dr/Dr_0 and $\eta_{0,sp}$ are computed using L = 1000 nm, d = 3 nm, and K = 1300 in eqs 1 and 2, respectively. The dashed blue line indicates $Dr/Dr_0 = 1$ and the colored area indicates the concentration above which the rods are confined in a tubelike confinement as envisioned by the DE theory.

MATERIALS AND METHODS

Materials. An aqueous CNC stock dispersion was purchased from CelluForce (NCV100, Montreal, Canada, pH 6.3). Two distinct OCNF (OCNF-L and OCNF-S) produced via TEMPO-mediated oxidation[45,46] were donated (Nippon Paper Group, Japan) as aqueous dispersions: OCNF-L with a degree of oxidation of 1.3−1.6 mmol/g, and OCNF-S with a degree of oxidation of 1.5−1.9 mmol/g. A Pf1 aqueous dispersion (10 mM K-phosphate buffer (pH 7.6), 2 mM $MgCl_2$ and 0.05% NaN_3) was purchased from ASLA biotech (Latvia). A 10 mg/mL XG aqueous stock was prepared via dissolution of XG powder (Keltrol T Plus, CP Kelco, Japan) in deionized water. Each concentration series was prepared gravimetrically using a micro-balance by the dilution of the respective stock. XG solutions and OCNF dispersions were prepared in deionized water. Pf1 dispersions were prepared in Tris-EDTA buffer (10 mM Tris-HCl, 1 mM disodium EDTA, pH 8.0, Sigma-Aldrich, BioUltra). CNC dispersions were prepared in a solvent composed of a glycerol:water mixture containing 60 vol % glycerol (Sigma-Aldrich, 99%). Glycerol was added to the aqueous solution to enhance the solvent viscosity and shift the onset of CNC alignment to lower shear rate values, extending the experimental window of measurable flow-induced alignment.

Steady Shear Rheo-Optical Measurements. Rheo-optical measurements were performed using a stress-controlled rheometer (Discovery HR-3, TA Instruments, U.S.A.) with a modular microscope accessory (MMA, TA Instruments, U.S.A.), schematically shown in Figure 2a. The rheometer is equipped with an upper Peltier plate (UPP, TA Instruments, U.S.A.) for temperature control and a glass bottom plate for optical access. A blue-light LED passes a linear polarizer before being focused at the upper rotating plate with a 5× objective lens. The beam is reflected by the top rotating plate (radius r = 20 mm), passes through the optically transparent bottom plate, an orthogonal linear polarizer (i.e., analyzer), and the image is recorded with a digital camera, in the given order. The top rotating plate is polished, with an estimate roughness of ∼100 nm to act as a mirror. Due to the crossed polarizers, only light that experiences a phase shift reaches the camera. Such a phase shift is caused by the birefringence

https://doi.org/10.1021/acs.biomac.3c00347
Biomacromolecules 2023, 24, 3304−3312

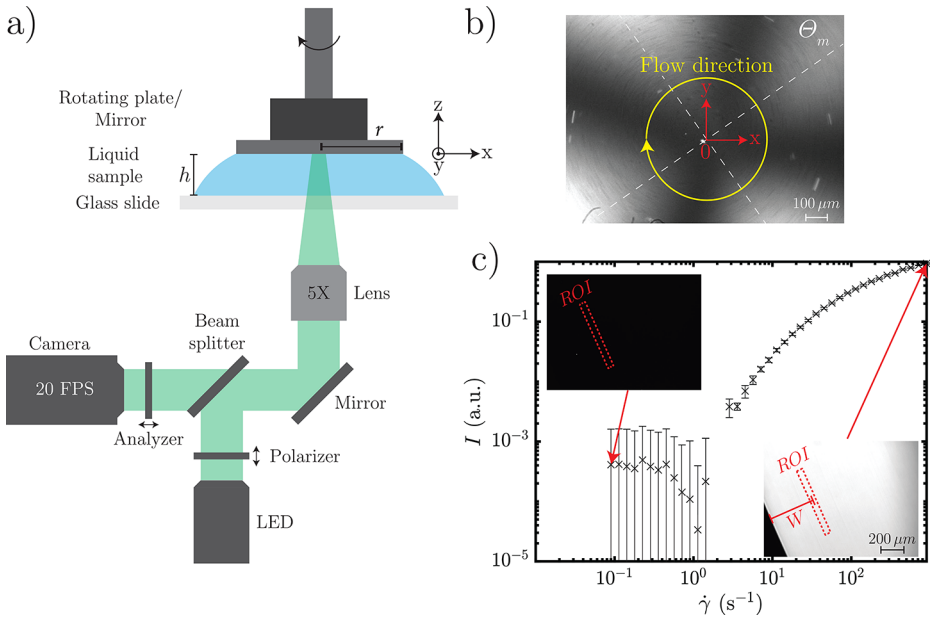

Figure 2. (a) Schematic of the rheo-optical setup. (b) Exemplary image acquired at the center of the plate ($x = y = 0$ mm) for a 4 mg/mL cellulose nanocrystals (CNC) dispersion in glycerol/water mixture (60 vol % glycerol) at a shear rate at the edge of the plate of $\dot{\gamma} = 900\ s^{-1}$. The flow direction is indicated by the yellow arrow. The dashed lines indicate the specific angle at which the light intensity is maximum (Θ_m). (c) Representative normalized intensity (I), after background subtraction, acquired in the region of interest (ROI) as a function of shear rate for a 5 mg/mL CNC dispersion in 60 vol % glycerol. The images for the lowest and highest shear rate ($\dot{\gamma} = 0.1$ and $900\ s^{-1}$) are shown as insets in (c).

of the fluid (Δn), associated in our experiments with a preferential orientation of the RC/RP. As the light enters perpendicular to the plate and thereby flow direction, this configuration probes the RC/RP projection in the vorticity-velocity plane (x–y plane, Figure 2). At a particular radial distance from the center of the plate (i.e., $x = y = 0$), the light intensity depends on the angle Θ along the circumference, yielding a typical cross-shaped pattern, as shown in Figure 2b for a representative sample.[47,48] Thus, at a given distance from the center of the plate along the Θ angle (e.g., the yellow arrow in Figure 2b), the probed light intensity follows a repeating increase-decrease trend with Θ. To increase sensitivity, the spatially averaged light intensity is measured at a specific angle Θ_m where the light intensity is maximum, as illustrated in Figure 2b by the dashed white lines. Additionally, to use the full range of the bit depth of the camera, intensity of the source LED light and pixel gain are adjusted for each sample. A region of interest (ROI) of rectangular shape located at a distance $W \approx 0.35$ mm from the edge of the plate (red rectangles in the insets of Figure 2c) is selected to retrieve the background subtracted and spatially averaged light intensity (I). Details of the measurement technique are included in the Supporting Information (Section S1). The ROI location is chosen to exploit the maximal shear rate while avoiding possible interference occurring at the edge of the plate due to the liquid–air interface and the liquid meniscus. Additionally, the ROI is chosen to be as parallel as possible to the edge of the rotating upper plate to minimize shear rate variation along the radial direction. Within the ROI, the shear rate experienced by the fluid element is $\dot{\gamma} \simeq \Omega(r - W)/h$, where Ω (rad/s) is the angular velocity of the rotating upper plate and h is the height of the sample (Figure 2a). The shear rate in the ROI is comparable to the shear rate at the edge of the plate $\left(\dot{\gamma} = \frac{\Omega r}{h}\right)$ computed by the software of the rheometer (TRIOS software, with ≈1.5% difference), thus we consider the shear rate at the edge of the plate as representative shear rate for both the rheological and the optical measurements. An exemplary measurement of the recorded, spatially averaged light intensity after background subtraction (I) as a function of shear rate ($\dot{\gamma}$) is shown in Figure 2c for 5 mg/mL CNC in a glycerol/water mixture containing 60 vol % glycerol.

The light intensity I at Θ_m is related to the birefringence Δn via

$$\Delta n = \frac{\lambda}{2\pi h} \arcsin\left(\sqrt{\frac{I}{I_{in}}}\right) \approx \frac{\lambda}{2\pi h}\sqrt{\frac{I}{I_{in}}} \quad (3)$$

with h the optical path, equal to the height of the sample (300 μm), I_{in} the intensity of the LED light source ($I_{in} \gg I$), and λ the wavelength of the light source.[47] Since h, λ, and I_{in} are kept constant in our experiment, $\Delta n \propto \sqrt{I}$. Additionally, $\Delta n \propto S$, where S is the structural order parameter obtained from rheo-SAS (small angle scattering) experiments, computed by the anisotropy of the two-dimensional scattering patterns,[49−52] hence, $\sqrt{I} \propto \Delta n \propto S$. This proportionality enables a direct comparison of our experiments with the literature on flow-induced birefringence and rheo-SAS of RC and RP fluids. The experimental window for $\sqrt{I}$ is limited by (i) the detectability of light above the background noise at relatively low RC/RP concentrations and relatively low shear rates and (ii) sensor saturation at relatively high RC/RP concentrations and high shear rates. Simultaneously to the optical measurements, the steady state shear viscosity (η) of the sample is obtained within an operational window set by the lower torque limit (0.2 μNm) at low shear rates and inertia limits at relatively high shear rates. All of the experiments were performed at 25 ± 0.01 °C.

RC and RP Characterizations. The morphology of the RC was characterized via atomic force microscopy (AFM, dimension ICON3 ScanAsyst, Bruker, U.S.A.). Dilute dispersions were deposited (~10 μL) on a freshly cleaved mica substrate (Mica AFM disk, Bruker, U.S.A.) and left at rest for ~60 s. Subsequently, the excess material was washed with deionized water and air-dried. For Pf1, the mica substrate was functionalized with (3-Aminopropyl)triethoxysilane (APTES) prior to their deposition as described by Diener et al.[53] Representative AFM images are shown in Figure 3 for Pf1 (a), CNC (b), OCNF-S (c), and OCNF-L (d). From imaging analysis, a characteristic contour length $\langle L \rangle$ (obtained from the volume averaged length, $\langle L \rangle = \frac{\sum_i^n L_i^4}{\sum_i^n L_i^3}$), the diameter d and the persistence length l_p of the rod-like particles were extracted (summarized in Table 1). Additionally, we defined a polydisperisty index as PDI = $\langle L \rangle / \langle L_n \rangle$, where $\langle L_n \rangle$ is the number-averaged contour length.[54] The RC and RP flexibility is captured by the number of persistence length segments per contour length, as $N_p = \langle L \rangle / l_p$. The persistence length, l_p,

https://doi.org/10.1021/acs.biomac.3c00347
Biomacromolecules 2023, 24, 3304−3312

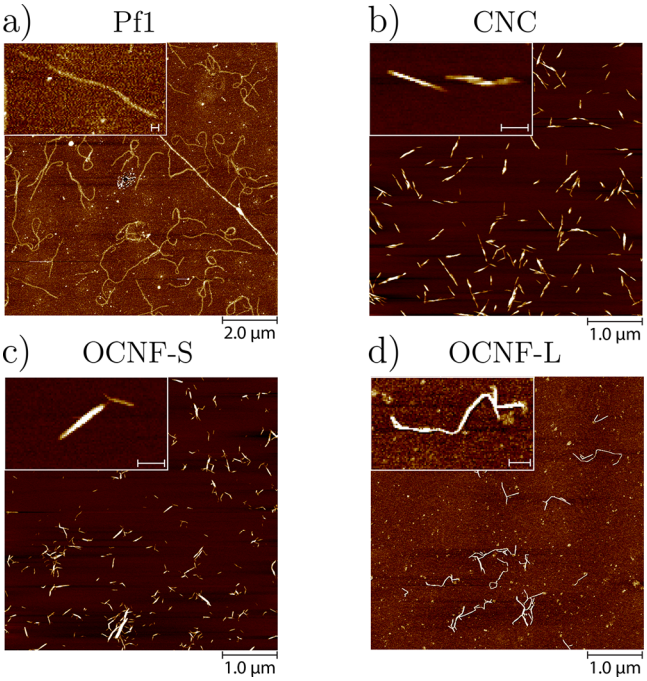

Figure 3. AFM (dimension ICON3 ScanAsyst, Bruker, U.S.A.) images of the rod-like colloids (RC) used in this study: (a) Pf1, (b) CNC, (c) OCNF-S, and (d) OCNF-L. The insets show exemplary RC with a scale bar of 100 nm.

Table 1. Relevant Parameters for the Biosourced RC and RP Used in This Work[a]

	Pf1	XG	OCNF-S	OCNF-L	CNC
$\langle L \rangle$ (nm)	1960	1651[54]	254	878	477
d (nm)	6.6[44]	2.1[58]	7.9	2.7	4.8
l_p (nm)	370	417[54]	704	222	7000
N_p	5.3	4.0	0.4	4.0	0.1
PDI	1.0	1.2[54]	1.7	2.0	1.8
c^* (mg/mL)	0.013	0.002	1.140	0.011	0.119
c^{**} (mg/mL)	3.97	1.50	36.64	3.62	11.86
c (mg/mL)	0.2−4	1−7	5−30	3−11	0.5−5

[a]Representative parameters for XG are obtained from literature. The range of concentrations (c) of RC and RP investigated via rheo-optics are given in the bottom row.

determining the length of the rigid rod-like segments composing the RC, was determined using the mean-squared end-to-end distance (MSED) method for a worm-like chain model within the FiberApp routine (details in Usov and Mezzenga[55]). Exclusively for XG, the characteristic dimensions are obtained from the literature because special experimental protocols are necessary for imaging of isolated XG chains using AFM, something that is outside the scope of the present study. From $\langle L \rangle$ and d, we estimate $c^* = \rho_p \pi d^2/(4\langle L \rangle^2)$ and $c^{**} = \rho_p \pi d/(4\langle L \rangle)$, respectively, by using a representative RC/RP density ρ_p = 1500 mg/mL for all the RC and RP investigated (Table 1).[44,56,57] We note that c^* and c^{**} must be regarded indicatively, as RC/RP flexibility and polydispersity are not considered in their estimation. To obtain structural information about the shear-induced RC and RP orientation, we investigated a concentration range that enables the measurement of the shear-dependent light intensity, $\sqrt{I}$, due to the fluid birefringence. These concentration ranges, summarized in Table 1, mainly fall in the semidilute regime, except for XG and OCNF-L, where the shear-dependent $\sqrt{I}$ was mostly measurable in the concentrated regime. For XG solutions at $c \gtrsim 2$ mg/mL, the pronounced excluded volume interactions were corroborated by the presence of nematic ordering of the sample at rest (see Supporting Information (Section S2)).

RESULTS AND DISCUSSION

Flow-Induced Alignment of RC and RP. Simultaneous measurements of the steady shear viscosity and fluid anisotropy for the RC dispersions and RP solutions are shown in Figure 4. Since $\sqrt{I}$ is linked with the number of aligned RC and RP through the optical path, we normalize the spatially averaged intensity as $\sqrt{I}/(c/c^*)$, referred to as reduced intensity (top row Figure 4).[59] To isolate the RC and RP contribution to the overall viscosity, we consider the specific viscosity, $\eta_{sp} = (\eta(\dot{\gamma}) - \eta_s)/\eta_s$ (bottom row of Figure 4). Generally, the reduced intensity increases with the increasing shear rate $\dot{\gamma}$ (top row in Figure 4). This indicates that more l_p segments of the RC and RP align preferentially with the flow as $\dot{\gamma}$ increases.[60] Specifically, $\sqrt{I}/(c/c^*)$ increases with a strong $\dot{\gamma}$-dependence around the onset of measurable intensity. Contrarily, at relatively high shear rates, $\sqrt{I}/(c/c^*)$ follows a less pronounced increase with $\dot{\gamma}$, indicating that the RC and RP approach the maximum extent of alignment. These two regimes are particularly evident for Pf1 dispersions at high concentrations, where $\sqrt{I}/(c/c^*)$ reaches a plateau at high values of $\dot{\gamma}$ (e.g., Pf1 at the highest concentration). Additionally, the onset of fluid anisotropy (i.e., $\sqrt{I} > 0$) shifts progressively to lower values of $\dot{\gamma}$ with the increasing RC and RP concentration. This is due to the increasing level of confinement experienced by each RC and RP as the concentration increases, resulting in a decreasing critical shear rate for the onset of RC/RP alignment. For the XG solutions with nematic ordering at rest (i.e., at the highest concentrations, $c/c^* > 1000$), the $\sqrt{I}/(c/c^*)$ as a function of the shear rate undergoes an abrupt change in slope at $\dot{\gamma} \approx 10^{-1}$ s^{-1}. This behavior is possibly associated with two distinct dynamical processes occurring at relatively low and high shear rates. At low shear rates, the sharp increase of $\sqrt{I}/(c/c^*)$ with the shear rate is linked to the simultaneous breakage/alignment of the nematic domains and the alignment of the XG backbone. Conversely, at high shear rates, the nematic domains break and the $\sqrt{I}/(c/c^*)$ trend can be associated uniquely to the alignment of XG backbone. These distinct dynamical processes occurring at relatively low and high shear rates are also supported by the presence of textured and homogeneous patterns in the raw images at low and high shear rates, respectively (see Supporting Information, Section S2).

From the rheological point of view, all dispersions are shear-thinning, characterized by a decreasing η_{sp} with increasing $\dot{\gamma}$ (bottom row, Figure 4). The most shear-thinning dispersions are the Pf1, XG, and OCNF-L, following a slope of ∼−3/4 for a large range of shear rate. In comparison, the shorter CNC and OCNF-S appear less shear thinning with a slope of ∼−1/3. We note that for all the systems investigated, the zero-shear viscosity plateau at $\dot{\gamma} \to 0$ (η_0) can not be probed within the operational window of the rheometer.

Specific Viscosity Scaling. To link the extent of RC and RP alignment (captured by $\sqrt{I}$) and the viscosity as a function of the shear rate, we plot the specific viscosity (η_{sp}) versus the reduced intensity ($\sqrt{I}/(c/c^*)$) in the top row of Figure 5. For all RC and RP investigated, the specific viscosity decreases with the increasing $\sqrt{I}/(c/c^*)$. Thus, as the extent of particle

https://doi.org/10.1021/acs.biomac.3c00347
Biomacromolecules 2023, 24, 3304−3312

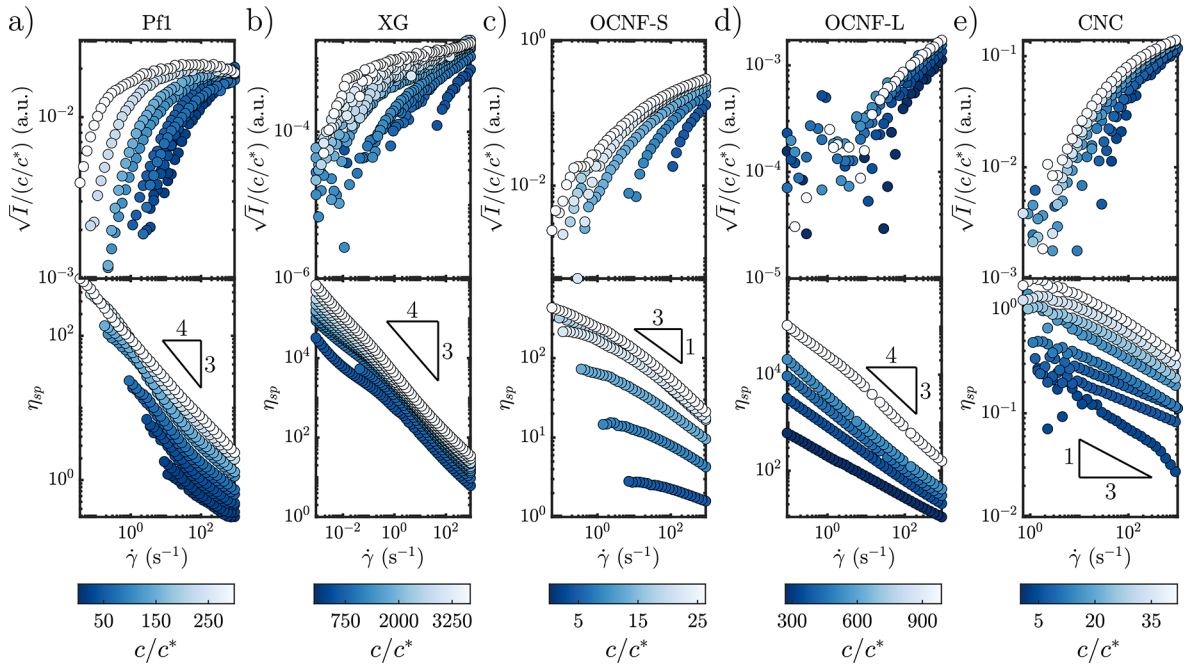

Figure 4. Reduced intensity $\sqrt{I}/(c/c^*)$ (top row) and specific viscosity η_{sp} (bottom row) as a function of shear rate, $\dot{\gamma}$: (a) Pf1, (b) XG, (c) OCNF-S, (d) OCNF-L, and (e) CNC at different concentrations, given in normalized form as c/c^*. The triangles in the bottom row indicate the reference slopes of η_{sp} as a function of $\dot{\gamma}$.

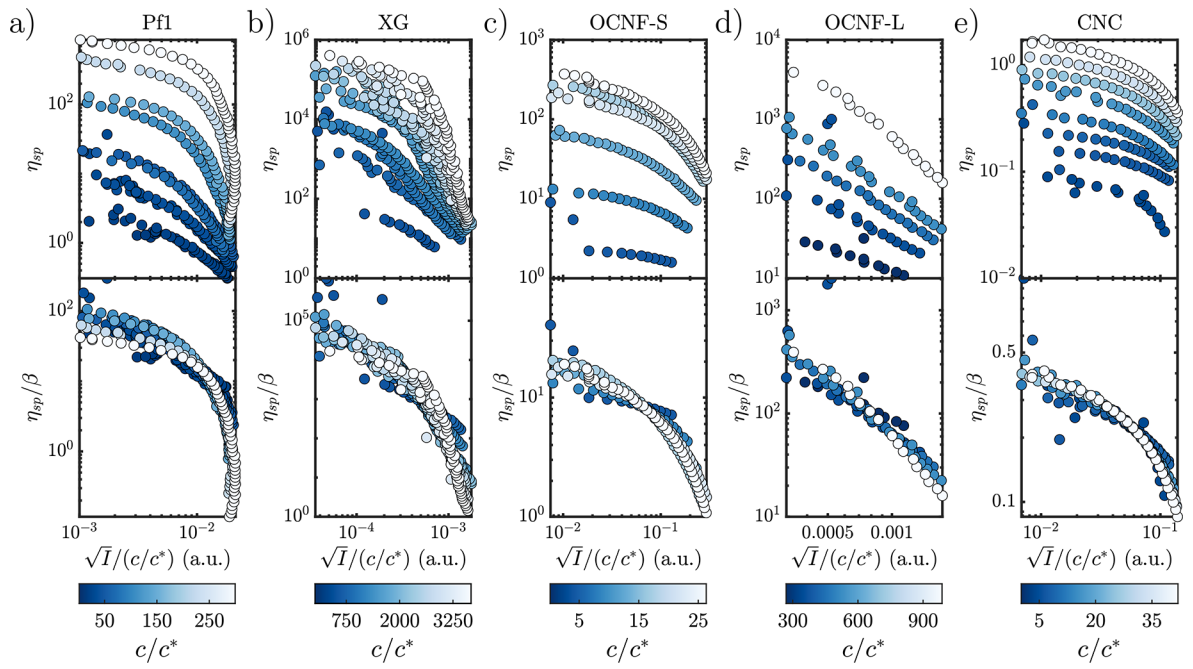

Figure 5. Specific viscosity η_{sp} (top row) and rescaled specific viscosity η_{sp}/β (bottom row) as a function of the reduced intensity $\sqrt{I}/(c/c^*)$, both obtained at matching values of shear rate. (a) Pf1, (b) XG, (c) OCNF-S, (d) OCNF-L, and (e) CNC at different concentrations given in normalized form as c/c^*.

alignment increases, the fluid viscosity decreases. In addition, for a given RC or RP system, the overall shape of the curves appears to be self-similar independently of the concentration. Thus, we try to collapse the viscosity data for each dispersion by introducing a scaling factor β to the specific viscosity, as η_{sp}/β (see bottom row in Figure 5). To determine the scaling factor β for each RC or RP system, a reference η_{sp} versus the respective $\sqrt{I}/(c/c^*)$ curve is chosen at an intermediate concentration, referred to as $\eta_{sp,ref}$. All the η_{sp} curves are then interpolated, and β is obtained for each concentration from the median of the ratio of the viscosity curves, $\eta_{sp}/\eta_{sp,ref}$. Since we keep our analysis at the scaling level, the choice of the reference curve ($\eta_{sp,ref}$) is arbitrary, and it does not significantly alter the β scaling.

The bottom row of Figure 5 shows the rescaled viscosity (η_{sp}/β) as a function of $\sqrt{I}/(c/c^*)$. For each RC and RP

https://doi.org/10.1021/acs.biomac.3c00347
Biomacromolecules 2023, 24, 3304−3312

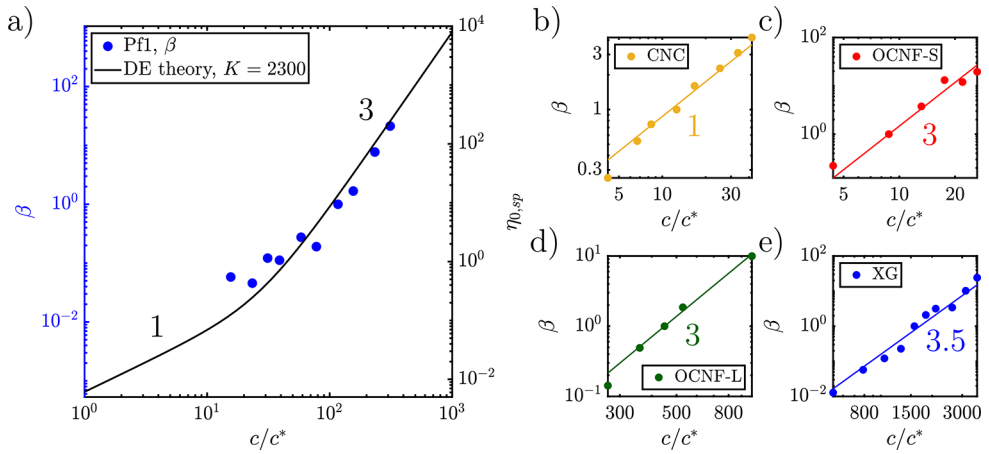

Figure 6. (a) Measured scaling factor β (left axis, blue symbols) as a function of Pf1 concentration (c/c^*) compared with the theoretical $\eta_{0,sp}$ based on eq 2 (right axis, black line). (b–e) Scaling factor β as a function of concentration c/c^* for the other RC and RP fluids investigated. The lines are power law fits describing the scaling of β with RC and RP concentration.

system, the curves obtained at different concentrations collapse into a master curve using the rescaled viscosity. Surprisingly, a single master curve captures each RC and RP systems well, ranging from the rigid CNC ($N_p < 1$) to the more flexible Pf1 and XG ($N_p > 1$), covering a wide concentration range. It is worth noting that all the RC and RP systems investigated share a similar trend of the reduced viscosity (η_{sp}/β) as a function of the reduced intensity ($\sqrt{I}/(c/c^*)$) despite their differences in contour length, flexibility, concentration range, and chemical composition (bottom row, Figure 5). This suggests that the relationship between the specific viscosity and the alignment of RC and RP is ruled by the same underlying mechanism. Specifically, our data can be described reasonably well with an exponential function at intermediate value of $\sqrt{I}$ (see Supporting Information, Section S3), in analogy to the exponential relationship between shear viscosity and the structural order parameter S obtained from rheo-SANS experiments on fd-viruses[30,31] and block copolymers.[29]

The idea of collapsing the η_{sp} versus $\sqrt{I}/(c/c^*)$ by introducing the scaling factor β to η_{sp} (as η_{sp}/β), is inspired by the method introduced by Förster et al.,[29] and later used by Lang et al.,[30,31] for the analysis of rheo-SANS experiments of RC dispersions. Specifically, they showed that by plotting η/η_0 as a function of S, the curves could collapse onto a single master curve for several concentrations within the semidilute regime. In the method introduced by Förster, η_0 is a scaling factor for the shear viscosity (i.e., η/η_0), analogously to the scaling factor β to η_{sp} in our analysis (i.e., η_{sp}/β); thus, we expect that $\beta \propto \eta_{0,sp}$.

We compare β obtained for the monodisperse Pf1 against the $\eta_{0,sp}$ prediction based on the DE theory using the known Pf1 dimensions (specified in Table 1) and K = 2300, as previously reported for Pf1, in eq 2 (Figure 6a).[31] Overall, the theoretical prediction captures the experimental trend, suggesting $\beta \propto \eta_{0,sp}$. At relatively high values of c/c^*, $\beta \propto (c/c^*)^3$ indicating interparticle confinement and that the tube assumption from the DE theory holds. As the concentration decreases, a scaling transition toward $\beta \propto c/c^*$ is approached due to the increased rotational freedom of the Pf1. For CNC, OCNF-S, OCNF-L, and XG we refrain from a quantitative comparison of β as a function of c/c^* with Doi's theory. The main challenge to quantitatively capture the scaling behavior for these systems stems from their polydispersity and the contribution that each size population has on the collective dynamics. As such, for these systems, we discuss the trend of β as a function of c/c^* only qualitatively. Given the proportionality $\beta \propto \eta_{0,sp}$, we interpret the β scaling with RC and RP concentrations in terms of confinement, analogously to $\eta_{0,sp}$ as a function of c/c^*. Specifically, a scaling of 1 (i.e., $\beta \propto c/c^*$) indicates an unconstrained rotational motion of the RC or RP, while a scaling of 3 (i.e., $\beta \propto (c/c^*)^3$) implies a constrained RC or RP rotational motion, where the DE tube assumption holds.

The scaling parameter β as a function of c/c^* for the other systems investigated are shown in Figure 6b–e. For CNC (Figure 6b), the data can be well described by the scaling of 1 ($\beta \propto c/c^*$), suggesting that within the concentration range investigated the CNC are not significantly interacting. Indeed, for the same CNC source, signature of interparticle interactions were only detected above our investigated concentration rage (i.e., $c \geq 5$ mg/mL).[61,62] For OCNF-S and OCNF-L, the data follow a scaling of 3 ($\beta \propto (c/c^*)^3$), suggesting a pronounced interparticle confinement as expected from the DE theory in the semidilute regime (Figure 6c,d).

It is important to note that although the different polydispersity ($2 \geq$ PDI ≥ 1) and flexibility ($5.3 \geq N_p \geq 0.1$) of the investigated RC systems, we recover the expected power law dependence with concentration according to Doi's theory (i.e., 1 and 3). This suggests that for concentrations below the onset of the nematic phase features of polydispersity and a small extent of flexibility, $N_p \sim 1$, can be still captured, at least qualitatively, within the "tube" framework. Differently from the exponent based on the DE theory in either the dilute and semidilute regime, the XG solutions follow the scaling of 3.5 ($\beta \propto (c/c^*)^{3.5}$). This is likely because most of the XG solutions investigated are in the concentrated regime with nematic ordering at rest (Supporting Information, Section S2).

CONCLUSIONS

We simultaneously measure the shear viscosity and flow-induced alignment of a library of biosourced rod-like colloids (RC) and rod-like polymers (RP) under rheometric shear flow. For each system, the specific viscosity η_{sp} follows a universal trend with the extent of the RC and RP alignment (as captured

https://doi.org/10.1021/acs.biomac.3c00347
Biomacromolecules 2023, 24, 3304–3312

by $\sqrt{I}$) that is concentration independent. We exploit this universality to retrieve β, a dimensionless parameter directly proportional to specific zero-shear viscosity, $\eta_{0,sp}$. For the RC fluids, we find good agreement of the $\eta_{0,sp}$ scaling as a function of concentration according to the Doi−Edwards theoretical prediction for rigid rods in the dilute and semidilute regime, regardless of the different polydispersity and flexibility of the investigated RC. Additionally, we find that, to some extent, the decreasing η_{sp} as a function of $\sqrt{I}$ can be captured by an exponential function for all the RC/RP fluids investigated. Although previous experiments have suggested such unique exponential decay of the shear viscosity as a function of RC alignment, we confirm that such a relationship is a general characteristic of RC and RP, independent of their polydispersity, aspect ratio, flexibility, and contour length. These results underlay the unique interlink between the flow-dependent rheological and structural properties of these liquids, providing solid guidelines for engineering processes involved with the controlled anisotropy of RC and RP fluids.

■ ASSOCIATED CONTENT

Supporting Information

The Supporting Information is available free of charge at https://pubs.acs.org/doi/10.1021/acs.biomac.3c00347.

Section S1 contains details on the measurement technique. Section S2 shows evidence of the presence of nematic ordering in XG solutions for the concentration range investigated. Section S3 shows the data presented in Figure 5 in a semilogarithmic representation (PDF)

■ AUTHOR INFORMATION

Corresponding Authors

Marvin Detert − *Physics of Fluids, Max Planck Center Twente for Complex Fluid Dynamics, and J. M. Burgers Centre for Fluid Dynamics, University of Twente, 7500 AE Enschede, The Netherlands; Physics of Interfaces and Nanomaterials, MESA+ Institute, University of Twente, 7500 AE Enschede, The Netherlands*; Email: marvin.w.detert@gmail.com

Vincenzo Calabrese − *Okinawa Institute of Science and Technology, Onna-son, Okinawa 904-0495, Japan*; orcid.org/0000-0001-5974-9217; Email: vincenzo.calabrese@oist.jp

Authors

Tatiana Porto Santos − *Okinawa Institute of Science and Technology, Onna-son, Okinawa 904-0495, Japan*; orcid.org/0000-0002-9768-2006

Amy Q. Shen − *Okinawa Institute of Science and Technology, Onna-son, Okinawa 904-0495, Japan*; orcid.org/0000-0002-1222-6264

Complete contact information is available at: https://pubs.acs.org/10.1021/acs.biomac.3c00347

Notes

The authors declare no competing financial interest.

■ ACKNOWLEDGMENTS

The authors acknowledge the support of Okinawa Institute of Science and Technology Graduate University with subsidy funding from the Cabinet Office, Government of Japan. M. D. acknowledges financial support from The Netherlands Center for Multiscale Catalytic Energy Conversion (MCEC), an NWO Gravitation programme funded by the Ministry of Education, Culture and Science of the government of The Netherlands and from the European Union's Horizon 2020 research and innovation programme under the Marie Skłodowska-Curie Grant Agreement No. 801359. V.C. acknowledges the financial support from the Japanese Society for the Promotion of Science (JSPS, Grant Number 22K14738). T.P.S. thanks Motif FoodWorks for the financial support. The authors thank CP Kelco for the donation of the XG and the Nippon Paper Group for the donation of OCNF-S and OCNF-L.

■ REFERENCES

(1) Helenius, G.; Bäckdahl, H.; Bodin, A.; Nannmark, U.; Gatenholm, P.; Risberg, B. In vivo biocompatibility of bacterial cellulose. *J. Biomed. Mater. Res., Part A* **2006**, *76*, 431−438.

(2) Klemm, D.; Kramer, F.; Moritz, S.; Lindström, T.; Ankerfors, M.; Gray, D.; Dorris, A. Nanocelluloses: A new family of nature-based materials. *Angew. Chem., Int. Ed.* **2011**, *50*, 5438−5466.

(3) Håkansson, K. M.; Fall, A. B.; Lundell, F.; Yu, S.; Krywka, C.; Roth, S. V.; Santoro, G.; Kvick, M.; Prahl Wittberg, L.; Wågberg, L.; et al. Hydrodynamic alignment and assembly of nanofibrils resulting in strong cellulose filaments. *Nat. Commun.* **2014**, *5*, 4018.

(4) Dumanli, A. G.; Van Der Kooij, H. M.; Kamita, G.; Reisner, E.; Baumberg, J. J.; Steiner, U.; Vignolini, S. Digital color in cellulose nanocrystal films. *ACS Appl. Mater. Interfaces* **2014**, *6*, 12302−12306.

(5) Mittal, N.; Ansari, F.; Gowda.V, K.; Brouzet, C.; Chen, P.; Larsson, P. T.; Roth, S. V.; Lundell, F.; Wågberg, L.; Kotov, N. A.; Söderberg, L. D. Multiscale Control of Nanocellulose Assembly: Transferring Remarkable Nanoscale Fibril Mechanics to Macroscale Fibers. *ACS Nano* **2018**, *12*, 6378−6388.

(6) Li, K.; et al. Alignment of Cellulose Nanofibers: Harnessing Nanoscale Properties to Macroscale Benefits. *ACS Nano* **2021**, *15*, 3646−3673.

(7) Shen, Y.; Levin, A.; Kamada, A.; Toprakcioglu, Z.; Rodriguez-Garcia, M.; Xu, Y.; Knowles, T. P. From Protein Building Blocks to Functional Materials. *ACS Nano* **2021**, *15*, 5819−5837.

(8) Thomas, B.; Raj, M. C.; B, A. K.; H, R. M.; Joy, J.; Moores, A.; Drisko, G. L.; Sanchez, C. Nanocellulose, a Versatile Green Platform: From Biosources to Materials and Their Applications. *Chem. Rev.* **2018**, *118*, 11575−11625.

(9) Kontturi, E.; Laaksonen, P.; Linder, M. B.; Nonappa; Gröschel, A. H.; Rojas, O. J.; Ikkala, O. Advanced Materials through Assembly of Nanocelluloses. *Adv. Mater.* **2018**, *30*, 1703779.

(10) Li, K.; Mcgrady, D.; Zhao, X.; Ker, D.; Tekinalp, H.; He, X.; Qu, J.; Aytug, T.; Cakmak, E.; Phipps, J.; Ireland, S.; Kunc, V.; Ozcan, S. Surface-modified and oven-dried microfibrillated cellulose reinforced biocomposites: Cellulose network enabled high performance. *Carbohydr. Polym.* **2021**, *256*, 117525.

(11) Dugan, J. M.; Collins, R. F.; Gough, J. E.; Eichhorn, S. J. Oriented surfaces of adsorbed cellulose nanowhiskers promote skeletal muscle myogenesis. *Acta Biomater* **2013**, *9*, 4707−4715.

(12) Abeer, M. M.; Mohd Amin, M. C. I.; Martin, C. A review of bacterial cellulose-based drug delivery systems: Their biochemistry, current approaches and future prospects. *J. Pharm. Pharmacol.* **2014**, *66*, 1047−1061.

(13) De France, K. J.; Yager, K. G.; Chan, K. J.; Corbett, B.; Cranston, E. D.; Hoare, T. Injectable Anisotropic Nanocomposite Hydrogels Direct in Situ Growth and Alignment of Myotubes. *Nano Lett.* **2017**, *17*, 6487−6495.

(14) Califano, D.; Kadowaki, M. A.; Calabrese, V.; Prade, R. A.; Mattia, D.; Edler, K. J.; Polikarpov, I.; Scott, J. L. Multienzyme cellulose films as sustainable and self-degradable hydrogen peroxide-producing material. *Biomacromolecules* **2020**, *21*, 5315−5322.

(15) Chen, L.; Remondetto, G. E.; Subirade, M. Food protein-based materials as nutraceutical delivery systems. *Trends Food Sci. Technol.* **2006**, *17*, 272−283.

(16) Li, F.; Biagioni, P.; Bollani, M.; Maccagnan, A.; Piergiovanni, L. Multi-functional coating of cellulose nanocrystals for flexible packaging applications. *Cellulose* **2013**, *20*, 2491−2504.
(17) Shen, Y.; Nyström, G.; Mezzenga, R. Amyloid Fibrils form Hybrid Colloidal Gels and Aerogels with Dispersed CaCO3 Nanoparticles. *Adv. Funct. Mater.* **2017**, *27*, 1700897.
(18) Pind'áková, L.; Kašpárková, V.; Bordes, R. Role of protein-cellulose nanocrystal interactions in the stabilization of emulsion. *J. Colloid Interface Sci.* **2019**, *557*, 196−206.
(19) Xiao, Y.; Liu, Y.; Wang, Y.; Jin, Y.; Guo, X.; Liu, Y.; Qi, X.; Lei, H.; Xu, H. Heat-induced whey protein isolate gels improved by cellulose nanocrystals: Gelling properties and microstructure. *Carbohydr. Polym.* **2020**, *231*, 115749.
(20) Zhao, S.; Chen, Z.; Dong, Y.; Lu, W.; Zhu, D. The Preparation and Properties of Composite Hydrogels Based on Gelatin and (3-Aminopropyl) Trimethoxysilane Grafted Cellulose Nanocrystals Covalently Linked with Microbial Transglutaminase. *Gels* **2022**, *8*, 146.
(21) Calabrese, V.; Shen, A. Q.; Haward, S. J. Naturally derived colloidal rods in microfluidic flows. *Biomicrofluidics* **2023**, *17*, 021301.
(22) Barry, E.; Beller, D.; Dogic, Z. A model liquid crystalline system based on rodlike viruses with variable chirality and persistence length. *Soft Matter* **2009**, *5*, 2563−2570.
(23) Colby, R. H. Structure and linear viscoelasticity of flexible polymer solutions: Comparison of polyelectrolyte and neutral polymer solutions. *Rheol. Acta* **2010**, *49*, 425−442.
(24) Shafiei-Sabet, S.; Hamad, W. Y.; Hatzikiriakos, S. G. Rheology of nanocrystalline cellulose aqueous suspensions. *Langmuir* **2012**, *28*, 17124−17133.
(25) Tang, H.; Kochetkova, T.; Kriegs, H.; Dhont, J. K.; Lettinga, M. P. Shear-banding in entangled xanthan solutions: Tunable transition from sharp to broad shear-band interfaces. *Soft Matter* **2018**, *14*, 826−836.
(26) Wyatt, N. B.; Liberatore, M. W. Rheology and viscosity scaling of the polyelectrolyte xanthan gum. *J. Appl. Polym. Sci.* **2009**, *114*, 4076−4084.
(27) Potier, M.; Tea, L.; Benyahia, L.; Nicolai, T.; Renou, F. Viscosity of aqueous polysaccharide solutions and selected homogeneous binary mixtures. *Macromolecules* **2020**, *53*, 10514−10525.
(28) Lang, C.; Lettinga, M. P. Shear flow behavior of bidisperse rodlike colloids. *Macromolecules* **2020**, *53*, 2662−2668.
(29) Förster, S.; Konrad, M.; Lindner, P. Shear thinning and orientational ordering of Wormlike Micelles. *Phys. Rev. Lett.* **2005**, *94*, 14−17.
(30) Lang, C.; Kohlbrecher, J.; Porcar, L.; Lettinga, M. P. The connection between biaxial orientation and shear thinning for quasi-ideal rods. *Polymers* **2016**, *8*, 291.
(31) Lang, C.; Kohlbrecher, J.; Porcar, L.; Radulescu, A.; Sellinghoff, K.; Dhont, J. K. G.; Lettinga, M. P. Microstructural Understanding of the Length- And Stiffness-Dependent Shear Thinning in Semidilute Colloidal Rods. *Macromolecules* **2019**, *52*, 9604−9612.
(32) Calabrese, V.; György, C.; Haward, S. J.; Neal, T. J.; Armes, S. P.; Shen, A. Q. Microstructural Dynamics and Rheology of Worm-like Diblock Copolymer Nanoparticle Dispersions under a Simple Shear and a Planar Extensional Flow. *Macromolecules* **2022**, *55*, 10031−10042.
(33) Santos, T. P.; Calabrese, V.; Boehm, M. W.; Baier, S. K.; Shen, A. Q. Flow-induced alignment of protein nanofibril dispersions. *J. Colloid Interface Sci.* **2023**, *638*, 487−497.
(34) Veerman, C.; Sagis, L. M. C.; Venema, P.; van der Linden, E. The effect of shear flow on the percolation concentration of fibrillar protein assemblies. *J. Rheol.* **2005**, *49*, 355−368.
(35) Haywood, A. D.; Weigandt, K. M.; Saha, P.; Noor, M.; Green, M. J.; Davis, V. A. New insights into the flow and microstructural relaxation behavior of biphasic cellulose nanocrystal dispersions from RheoSANS. *Soft Matter* **2017**, *13*, 8451−8462.
(36) Orts, W. J.; Godbout, L.; Marchessault, R. H.; Revol, J.-F. Enhanced ordering of liquid crystalline suspensions of cellulose microfibrils: a small angle neutron scattering study. *Macromolecules* **1998**, *31*, 5717−5725.
(37) Lane, C.; Rode, D.; Rösgen, T. Birefringent properties of aqueous cellulose nanocrystal suspensions. *Cellulose* **2022**, *29*, 6093−6107.
(38) Lane, C.; Rode, D.; Rösgen, T. Optical characterization method for birefringent fluids using a polarization camera. *Opt. Lasers Eng.* **2021**, *146*, 106724.
(39) Fjodorova, J.; Held, R.; Hublik, G.; Esteban Vazquez, J. M.; Walhorn, V.; Hellweg, T.; Anselmetti, D. Tuning Xanthan Viscosity by Directed Random Coil-to-Helix Transition. *Biomacromolecules* **2022**, *23*, 4493−4503.
(40) Rodd, A. B.; Dunstan, D. E.; Boger, D. V. *Hydrocolloids*; Elsevier, 2000; pp 151−157.
(41) Doi, M.; Edwards, S. F. Dynamics of rod-like macromolecules in concentrated solution. Part 1. *J. Chem. Soc., Faraday Trans. 2* **1978**, *74*, 560−570.
(42) Doi, M.; Edwards, S. F. *The Theory of Polymer Dynamics*; Oxford University Press: New York, 1988.
(43) Teraoka, I.; Ookubo, N.; Hayakawa, R. Molecular Theory on the Entanglement Effect of Rodlike Polymers. *Phys. Rev. Lett.* **1985**, *55*, 2712−2715.
(44) Barabé, B.; Abakumov, S.; Gunes, D. Z.; Lettinga, M. P. Sedimentation of large particles in a suspension of colloidal rods. *Phys. Fluids* **2020**, *32*, 053105.
(45) Saito, T.; Kimura, S.; Nishiyama, Y.; Isogai, A. Cellulose Nanofibers Prepared by TEMPO-Mediated Oxidation of Native Cellulose. *Biomacromolecules* **2007**, *8*, 2485−2491.
(46) Shinoda, R.; Saito, T.; Okita, Y.; Isogai, A. Relationship between Length and Degree of Polymerization of TEMPO-Oxidized Cellulose Nanofibrils. *Biomacromolecules* **2012**, *13*, 842−849.
(47) Mykhaylyk, O. O.; Warren, N. J.; Parnell, A. J.; Pfeifer, G.; Laeuger, J. Applications of shear-induced polarized light imaging (SIPLI) technique for mechano-optical rheology of polymers and soft matter materials. *J. Polym. Sci., Part B: Polym. Phys.* **2016**, *54*, 2151−2170.
(48) Kádár, R.; Spirk, S.; Nypelo, T. Cellulose nanocrystal liquid crystal phases: Progress and challenges in characterization using rheology coupled to optics, scattering, and spectroscopy. *ACS Nano* **2021**, *15*, 7931−7945.
(49) van Gurp, M. The use of rotation matrices in the mathematical description of molecular orientations in polymers. *Colloid Polym. Sci.* **1995**, *273*, 607−625.
(50) Purdy, K. R.; Dogic, Z.; Fraden, S.; Rühm, A.; Lurio, L.; Mochrie, S. G. Measuring the nematic order of suspensions of colloidal fd virus by x-ray diffraction and optical birefringence. *Phys. Rev. E* **2003**, *67*, 031708.
(51) Rosén, T.; Wang, R.; Zhan, C.; He, H.; Chodankar, S.; Hsiao, B. S. Cellulose nanofibrils and nanocrystals in confined flow: Single-particle dynamics to collective alignment revealed through scanning small-angle x-ray scattering and numerical simulations. *Phys. Rev. E* **2020**, *101*, 032610.
(52) Uetani, K.; Koga, H.; Nogi, M. Estimation of the Intrinsic Birefringence of Cellulose Using Bacterial Cellulose Nanofiber Films. *ACS Macro Lett.* **2019**, *8*, 250−254.
(53) Diener, M.; Adamcik, J.; Bergfreund, J.; Catalini, S.; Fischer, P.; Mezzenga, R. Rigid, Fibrillar Quaternary Structures Induced by Divalent Ions in a Carboxylated Linear Polysaccharide. *ACS Macro Lett.* **2020**, *9*, 115−121.
(54) Camesano, T. A.; Wilkinson, K. J. Single Molecule Study of Xanthan Conformation Using Atomic Force Microscopy. *Biomacromolecules* **2001**, *2*, 1184−1191.
(55) Usov, I.; Mezzenga, R. FiberApp: An open-source software for tracking and analyzing polymers, filaments, biomacromolecules, and fibrous objects. *Macromolecules* **2015**, *48*, 1269−1280.
(56) Wagner, R.; Raman, A.; Moon, R. Transverse Elasticity of Cellulose Nanocrystals Via atomic Force microscopy, 10th International Conference on Wood & Biofiber Plastic Composites; 2010; pp

https://doi.org/10.1021/acs.biomac.3c00347
Biomacromolecules 2023, 24, 3304−3312

309−316. https://engineering.purdue.edu/nanotrees/files/WagnerR-2010_Transverse_Elasticity_of_CNC_by_AFM.pdf
(57) Eichhorn, S. J. Cellulose nanowhiskers: Promising materials for advanced applications. *Soft Matter* **2011**, *7*, 303−315.
(58) Moffat, J.; Morris, V. J.; Al-Assaf, S.; Gunning, A. P. Visualisation of xanthan conformation by atomic force microscopy. *Carbohydr. Polym.* **2016**, *148*, 380−389.
(59) Calabrese, V.; Varchanis, S.; Haward, S. J.; Shen, A. Q. Alignment of Colloidal Rods in Crowded Environments. *Macromolecules* **2022**, *55*, 5610−5620.
(60) Nijenhuis, K.; McKinley, G.; Spiegelberg, S.; Barnes, H.; Aksel, N.; Heymann, L.; Odell, J. In *Springer Handbook of Experimental Fluid Mechanics*; Tropea, C., Yarin, A. L., Foss, J. F., Eds.; Springer: Berlin, Heidelberg, 2007; pp 619−743.
(61) Bertsch, P.; Sánchez-Ferrer, A.; Bagnani, M.; Isabettini, S.; Kohlbrecher, J.; Mezzenga, R.; Fischer, P. Ion-Induced Formation of Nanocrystalline Cellulose Colloidal Glasses Containing Nematic Domains. *Langmuir* **2019**, *35*, 4117−4124.
(62) Cainglet, H. E.; Tanner, J.; Nasiri, N.; Browne, C.; Garnier, G.; Batchelor, W. Rapid cellulose nanomaterial characterisation by rheology. *Cellulose* **2023**, *30*, 4971−4982.

https://doi.org/10.1021/acs.biomac.3c00347
Biomacromolecules 2023, 24, 3304−3312